Int. J. Electrochem. Sci., 8 **(2013)** 4085 - 4097

International Journal of
ELECTROCHEMICAL
SCIENCE
www.electrochemsci.org

Initial Corrosion Processes and Mechanism of 23Co14Ni12Cr3Mo Ultra-high Strength Steel in Salt Spray Environment

J. H. Liu[*], *C. Wen, M. Yu, S. M. Li, B. Wang*

School of Materials Science and Engineering, Beihang University, Beijing, 100191, China
[*]E-mail: liujh@buaa.edu.cn

Received: 9 January 2013 / *Accepted:* 13 February 2013 / *Published:* 1 March 2013

The initial corrosion processes and mechanism of 23Co14Ni12Cr3Mo Ultra-high Strength steel were researched by using salt spray test (SST) and electrochemical methods. The corrosion morphologies were observed by optical microscope, scan electron microscope (SEM), and atomic force microscopy (AFM). And the corrosion products were characterized by energy dispersive spectrometer (EDS), x-ray diffraction (XRD), Fourier transform infrared spectroscopy (FT-IR), and x-ray photoelectron spectroscopy (XPS).The results showed that the corrosion happens from pits and forms two layers for 96h. The corrosion products continuously transform from staked granular to acicular, and finally to sintered. The oxides of Fe are transformed in the form of Fe ion to γ-FeOOH, to α-FeOOH or Fe_2O_3, and finally to Fe_3O_4.The corrosion mechanism and the corrosion growth model were also studied combined the morphology results, corrosion product analysis and electrochemical results.

Keywords: 23Co14Ni12Cr3Mo; ultra-high strength steel; Initial corrosion; mechanism; salt spray

1. INTRODUCTION

The ultra-high strength steel 23Co14Ni12Cr3Mo is developed in high-performance aerospace applications that require high tensile strength and fracture toughness [1-2]. However, the corrosion resistance of 23Co14Ni12Cr3Mo steel is still an issue due to its low chromium content and the presence of carbide and intermetallic precipitates formed during heat treatment [3]. Most of the attentions were paid to influence of hydrogen [4-5], stress corrosion behaviors[6-7] and electrochemical behaviors[3,8] in recent years. In order to understand the contribution of corrosion on performance of the steel, it is important to study the initial corrosion process and mechanism especially the evolution of pits of the steel.

Salt spray testing is one of the main techniques for initial corrosion studies [9].Yang [10] investigated the corrosion behavior by SST, which obtained a three-stage corrosion process for the corrosion behavior. Liu [11] investigated the corrosion morphology, composition, and maximum mean corrosion depth in neutral salt spray environment. Zhao [12] evaluated the effect of the surface film on salt-spray corrosion behaviors by measuring hydrogen evolution and estimated the corrosion rate.

Our previous studies[13-15] have been studied the corrosion behavior of high strength steels in neutral salt spray test (NSST), which obtained the composition of corrosion products of this steels and the effect of NSST on mechanical properties. In this paper, the evolution of pits and elements of corrosion products in the surface of 23Co14Ni12Cr3Mo steel was studied in salt spray environment in the initial corrosion of the steel by optical microscope, scan electron microscope (SEM), and atomic force microscopy (AFM). The corrosion products were characterized by energy dispersive spectrometer (EDS), x-ray diffraction (XRD), Fourier transform infrared spectroscopy (FT-IR), and x-ray photoelectron spectroscopy (XPS).

2. EXPERIMENTAL

2.1 Material

The chemical composition (in wt. %) of 23Co14Ni12Cr3Mo steel is as follows: 0.23C, 13.4Co, 11.1Ni, 3.1Cr and Fe balance. The heat treatment was solution treatment for 5h at 885±5°C, air cooling to 92°C in 2h, freezing for 1h at -73°C, aging for 5h at 482°C, and air cooling to room temperature. The mechanical properties following this heat treatment were given in table 1.

Table 1. Mechanical properties of ultra-high strength steel 23Co14Ni12Cr3Mo

Material	σ_b(MPa)	$\sigma_{0.2}$(MPa)	δ_5(%)	ψ(%)	K_{IC}(MPa•m$^{0.5}$)
23Co14Ni12Cr3Mo	1960	1690	14	68.5	136

2.2 Experiment procedure

Specimens(50×40×3mm) were subsequently ground with 150, 280, 500, and 1000 grit silicon carbide papers and then sealed by chloroprene rubber with an exposure area for 40×40mm. Corrosion resistances of the ultra-high strength steel was evaluated by the salt spray test, which was used to simulate the atmospheric environment. The salt spray test was followed by the standard ASTM B117-97. The samples were tested for at 35±2 °C in the salt spray of 5wt% neutral sodium chloride solution with salt spray settlement 1~2ml/80cm^2.h.

2.3 Morphology observation and composition analysis

The corrosion and cross section morphology of specimens tested for different time were characterized by optical microscope, SEM (CS3400, Britain) and AFM (vecoo, America). The corrosion products were analyzed by XRD (D/MAX-2200pc, Cu K_α, Japan), EDS (CS3400) and FT-IR (nicolet6700, America).

2.4 Polarization curves measurement

A Princeton applied research (PAR) Electrochemical work system 2273 was used for all the electrochemical measurements. The working electrode employed (φ10×2.5mm) were polished to 1000 grinds, Reference electrode (Saturated Calomel Electrode) for 30 min provided a reproducible initial surface condition. The electrochemical impedance spectroscopy (EIS) tests were performed at open-circuit potential (OCP) with a rms signal of 10mV amplitude and at frequencies ranging from 100KHz to 10mHz. The potentiodynamic experiments were performed from−0.5 V vs OCP up to 0.5V vs OCP with scan rate of 0.5 mV s^{-1}. The EIS data was analyzed using the commercial software ZimpWin.

3. RESULTS AND DISCUSSION

3.1 Corrosion morphology

Fig.1 shows the corrosion morphologies by optical microscopy. It is notable that the corrosion source forms as the specimens immersed in salt spray camber for about 10min. The pit enlarges its size and develops in depth after it appears. For a longer time, the surface of the specimen is covered by corrosion products. The corrosion products become thicker, and transform to loose tissues.

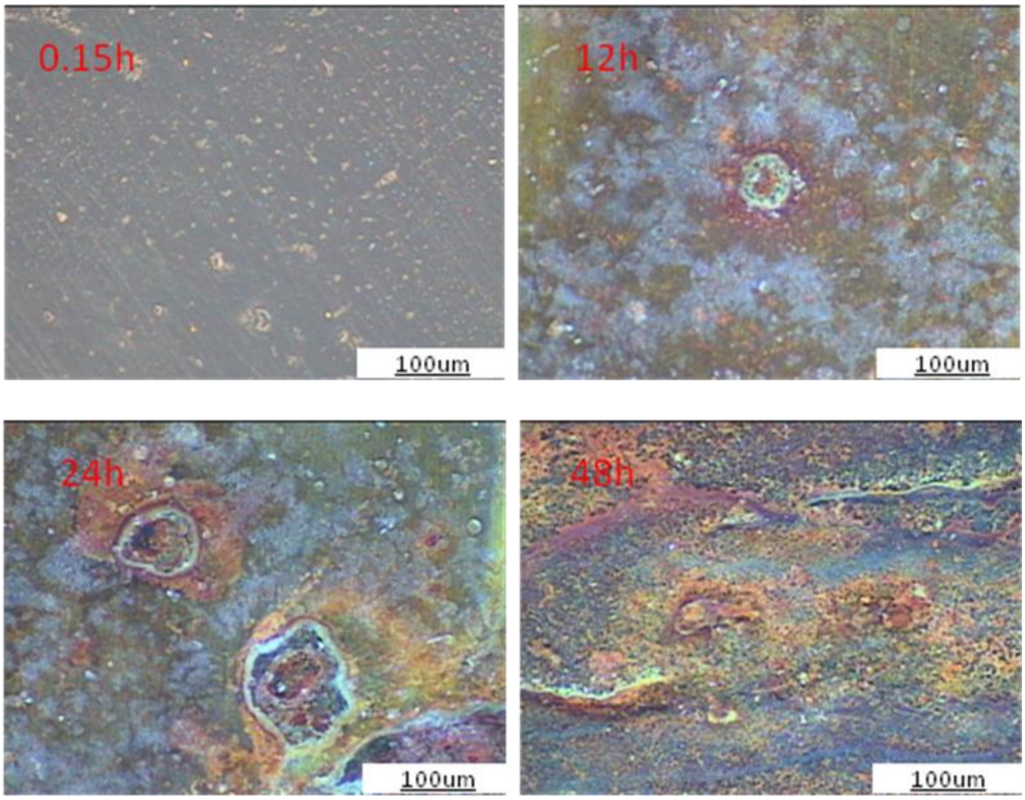

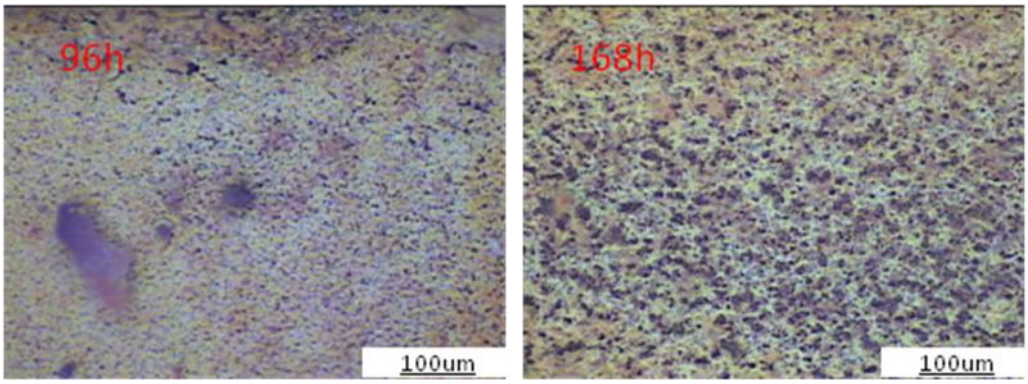

Figure 1. Optical micrographs with different time of 23Co14Ni12Cr3Mo steel

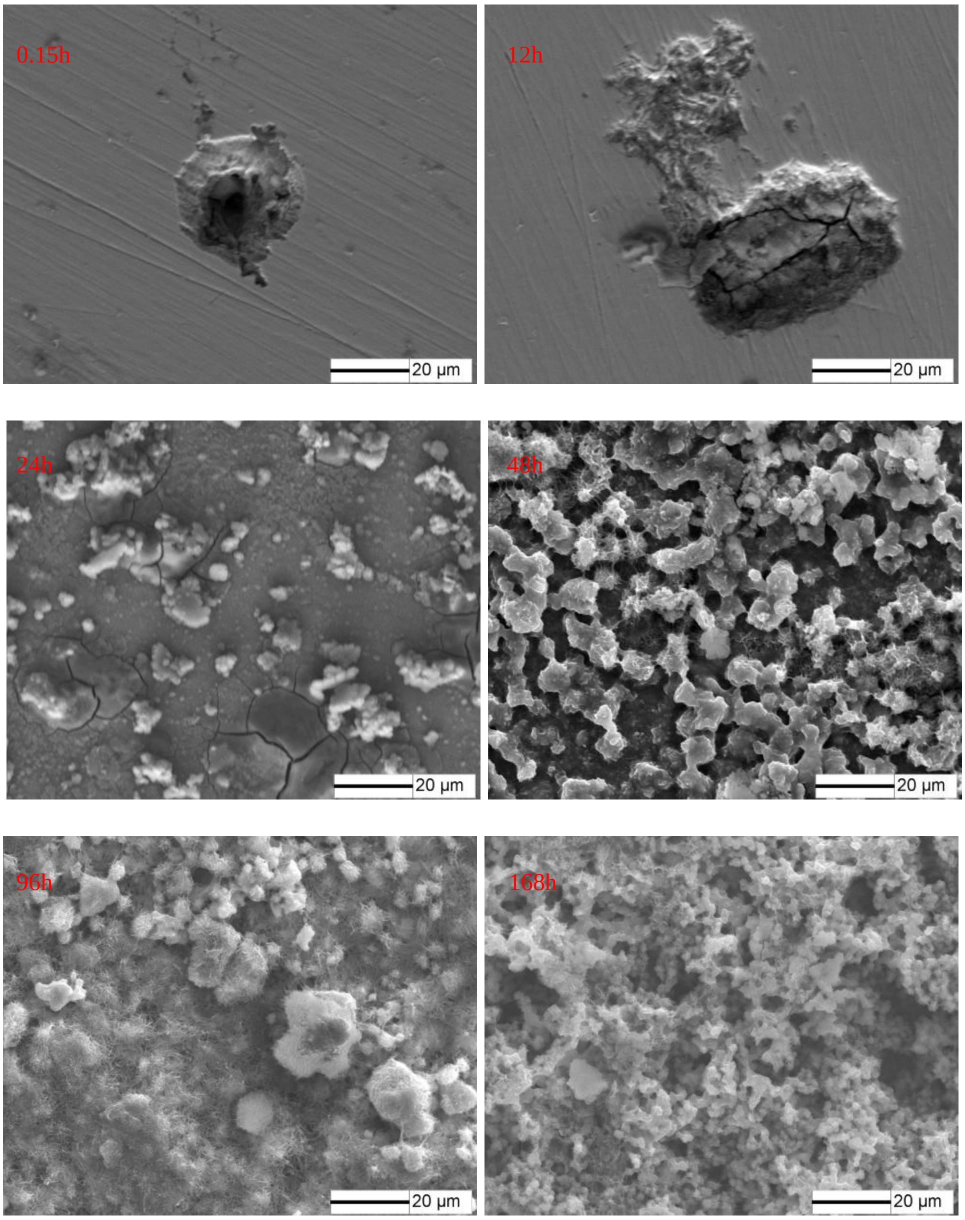

Figure 2. SEM micrographs of the surface of 23Co14Ni12Cr3Mo steel

SEM micrographs of the corrosion scales of 23Co14Ni12Cr3Mo steel in salt spray test are shown in Fig.2. The ions enters the surface of the specimens, which leads to surface bubbling (0.15h).The bubbles grow and micro cracks form in the surfaces. Rupture of the cracks formed pits. The pits grown up and merging each other, finally form rugged general corrosion covering the whole surface (48h). Except the metal corrosion, the corrosion products continuously transform from staked granular to acicular, and finally to sintered.

3.2 Cross section morphology

Fig.3 show the cross section morphologies for different testing time of 23Co14Ni12Cr3Mo steel in SST. From the cross section morphologies, it can be observed that the micro cracks emerge in the corrosion product layer in the first two days. This is due to the loose and flaky corrosion products formed in initial stage of corrosion. However, after corrosion for 96h, the corrosion products display two layers, the inner lay and outer layer. The outer layer seems to be denser than the inner layer. The corrosion product layer are consisted of the dense lay close to the matrix and the loose layer in the specimen surface after corrosion for 168h.The difference of the corrosion products between the inner and outer layers for 96h and 168h implies a transform in the corrosion products.

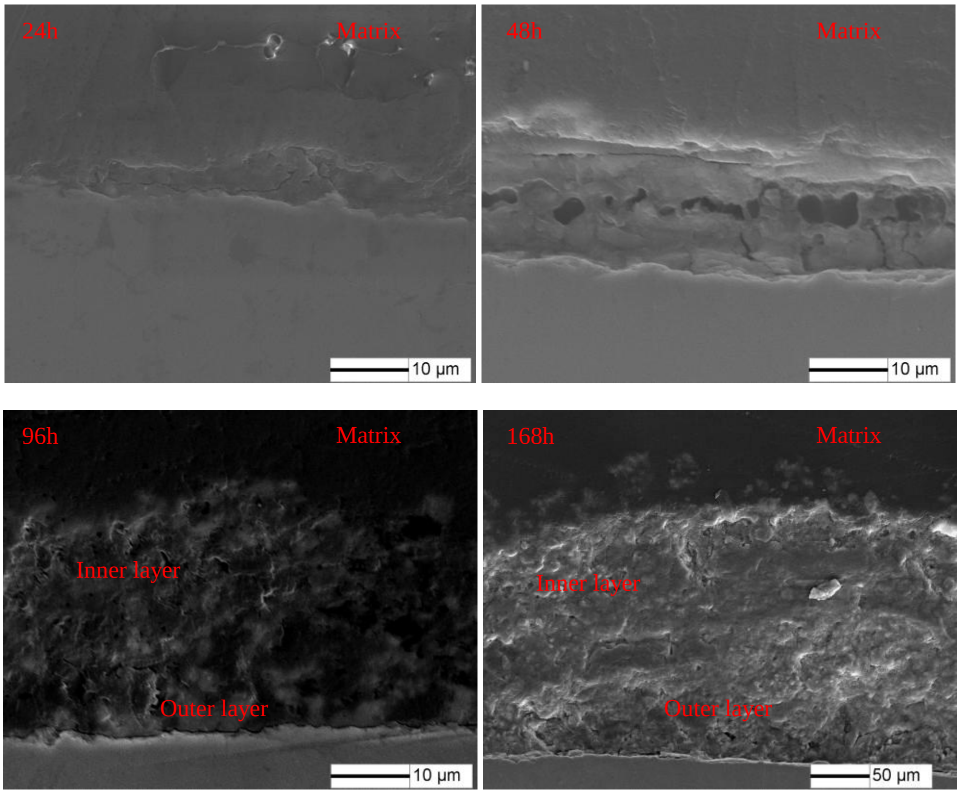

Figure 3. Cross section morphology of 23Co14Ni12Cr3Mo steel immersed in SST for different time

3.3 Corrosion products analysis

The EDS results of 23Co14Ni12Cr3Mo steel from the corrosion surface and corrosion layer in cross section are given in Table 2. The surface element detected by area scan and the cross section element detected by point scan. The content of Cr (%) trends to be decreasing with testing time in the surface while increasing in the cross section. It is indicated that the element Cr is mainly enriched in the interface of initial corrosion products and matrix, which may stop the corrosion further developing. The surface contents of Co and Ni decrease before 48h and from 48h~168h, while show a high content for 48h. The cross section contents of Co and Ni trend to be increasing with the testing time, and both are below the matrix content. It is illustrated that the elements Co and Ni participate in the corrosion.

Table 2. Element contents of corrosion products of 23Co14Ni12Cr3Mo steel by EDS

Region	Time(h)	C(%)	O(%)	Cr(%)	Fe(%)	Co(%)	Ni(%)	Cl(%)	Na(%)
Surface	1			3.07	58.22	11.71	9.26	1.33	3.13
	3		1.75	1.91	39.34	7.71	6.08	12.77	26.6
	6		21.73	1.22	50.12	7.5	4.98	9.96	4.5
	24		26.54	0.33	60.33	1.68	0.95	6.24	2.96
	48		13.93		29.35	8.76	8.38	21.29	18.29
	96		18.47		30.44	4.72	3.7	23.04	19.62
	168		15.18		37.46	3.87	2.14	28.48	19.88
Cross section	6	26.45	12.10	0.77	47.18	4.14	3.18	0.77	
	24	28.60	5.56	1.25	52.60	3.58	2.56		
	48	13.35	6.17	13.63	29.89	6.78	10.45		
	96	6.97	1.85	16.34	34.11	8.37	10.25		
	168		4.12	8.39	47.51	11.71	11.04		

Fig.4 summarizes the FT-IR absorbance spectra of primer films for different time in SST exposure, respectively. From Fig.4 (a), the spectrum taken in the location in front of the delamination contains 3 characteristic bands at 3429.20, 2921.79 and 2852.16 cm^{-1} which are related to stretching vibrations of O–H bonds. The band at 611.41cm^{-1} is related to stretching vibration of Fe-O bond [16]. It is clarified that the oxide FeOOH is formed in all corrosion products of 23Co14Ni12Cr3Mo steel in SST for different time. In order to identify the divergence of the corrosion products for different time, detail plot from 700cm^{-1}~2000cm^{-1} is shown in Fig.4 (b). The corrosion products for 24h contain of deformation vibrations of O–H bonds corresponding to γ-FeOOH. No obvious divergence is found for the corrosion products testing for 48h except for a salient peak in 1166.01cm^{-1} (A) which is related to γ-FeOOH. After immersed for 96h, the band A disappears and 2 characteristic bands at 805.13 and 2852.16 cm^{-1} corresponding to α-FeOOH are found. The broad bands at A and B are attenuated for 168h. It is reveal that the corrosion products exist the transforms of γ-FeOOH to α-FeOOH, and α-FeOOH to other oxides of Fe.

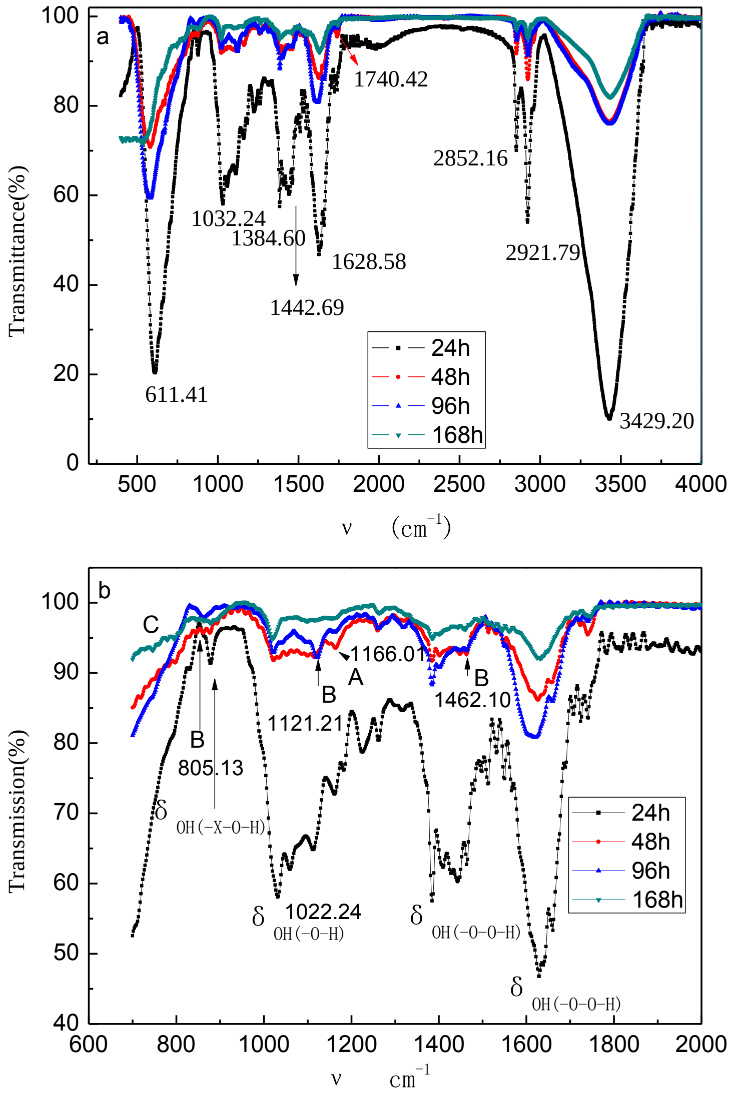

Figure 4. FT-IR curves of the corrosion products removed from the steel (b is plot of a form 700cm^{-1}~200cm^{-1})

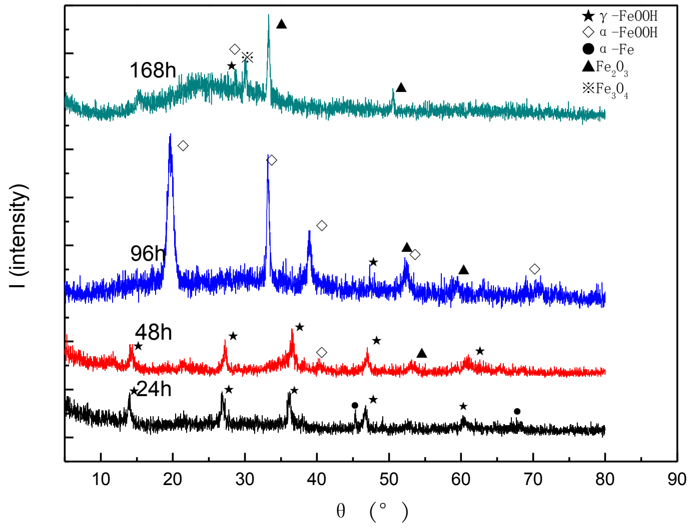

Figure 5. XRD patterns of the corrosion products removed from the steel after exposure to SST for different time

X-ray diffraction patterns of the corrosion products removed from the steel for different time are displayed in Fig.5.At the initial stage of SST, the corrosion products are mainly consisted of γ-FeOOH, some of which transform to α-FeOOH and Fe_2O_3 from 48h to 96h.After testing for 168h, the corrosion products are mainly consisted of α-FeOOH, Fe_2O_3 and Fe_3O_4. Combined with the FT-IR results, it demonstrated the oxides of Fe are transformed in the form of Fe to γ-FeOOH, to α-FeOOH or Fe_2O_3, and finally to Fe_3O_4.

The XPS peaks of oxides of 23Co14Ni12Cr3Mo steel for 168 h in SST are shown in Fig. 6. The corrosion products contain oxides of Fe and Co, and NaCl. The main element of Fe is identified from the XPS spectra of corrosion product. Of the two peaks of Fe2p Fe 2p3/2 peak is narrower and stronger than Fe 2p1/2 because in spin orbit (j-j) coupling. The peak position of Fe 2p3/2 and Fe 2p1/2 are 710.75 and 724.1 eV, respectively, which is corresponding to Fe_3O_4 [17]. It demonstrated that after testing for 168h, the corrosion products are mainly consisted of Fe_3O_4.

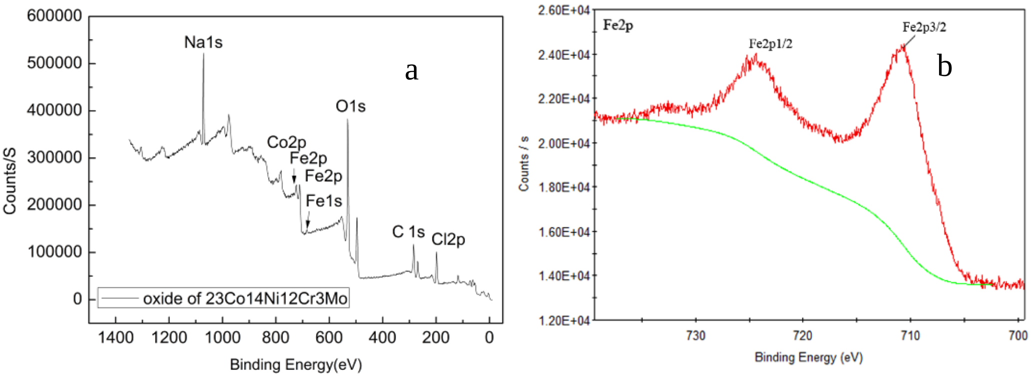

Figure 6. XPS spectra of oxides of 23Co14Ni12Cr3Mo steel for 168 h in SST after background subtraction (a: XPS spectra, b: Fe2p)

3.4 Electrochemical measurements

The results of Nyquist plot as a function of exposure time in solutions and its related electrochemical equivalent circuits are presented in Fig.7. Here, R_l refers to the solution resistance, Q_c refers to constant phase element of the electric double layer, R_c refers to the charge transfer resistance, Q_f refers to the constant phase element of the corrosion product layer and R_f refer to the resistance of the corrosion product layer [3,13]. The electric element Q_f/s R_f/s refers to processes occurring at the corrosion product layer /metal interface, and Q_c/s R_c/s refers to processes occurring at the corrosion product layer/solution interface. Using the circuit, the EIS data were fitted and the summary of the results for different time is presented in Table 3.It can be obtained that before SST, the reaction of the specimen are easy and quick, and no corrosion product barrier formed in the specimen surface. After immersed in SST, the corrosion product layer forms and protects the substrate from corrosion. As a result, R_{ct} becomes bigger as the SST continues further. The corrosion product layer becomes thicker as the SST continues, and when reaches to 168h, the layer forms a barrier of ions transformation (Fig.7(c)). The EIS results suggest that the corrosion products reduce the corrosion rate.

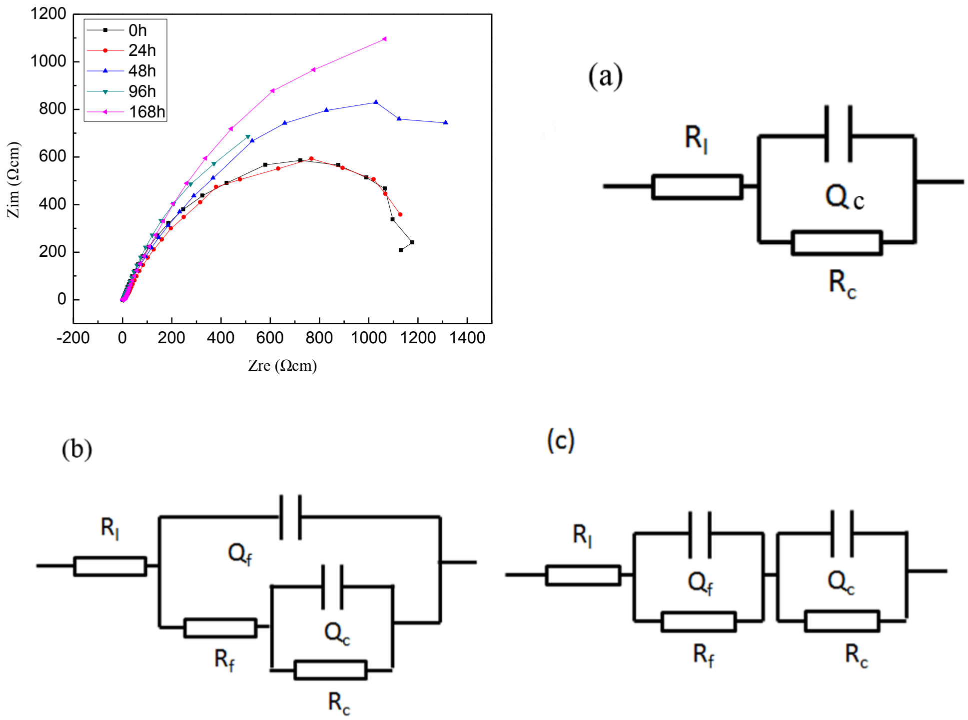

Figure 7. EIS plots of 23Co14Ni12Cr3Mo after SST for different time (a is the EIS results and b, c, d are the electrochemical equivalent circuit for 0h, 24~96h, 168h, respectively)

Table 3. Values of parameters calculated from Nyquist diagrams

Times(h)	$R_l(\Omega cm^2)$	$Q_{dl}(\Omega^{-1}s^ncm^2)$	n	$R_f(\Omega cm^2)$	$Qc(\Omega^{-1}s^ncm^2)$	n	$Rc(\Omega cm^2)$
0	1.577				2.000×10^{-3}	0.794	1539
24	0.713	3.719×10^{-3}	0.816	16.08	2.241×10^{-3}	0.746	1649
48	0.711	5.962×10^{-4}	0.842	11.33	3.322×10^{-3}	0.792	2709
96	0.620	3.605×10^{-3}	0.802	2.88	6.448×10^{-3}	0.817	2844
168	0.772	7.207×10^{-4}	0.815	10.45	5.029×10^{-3}	0.794	3552

Fig.8 shows the potentiodynamic polarization curves of 23Co14Ni12Cr3Mo after SST for different time. The parameters from polarization curves are listed in Table 4. The corrosion potentials E_{corr} of the specimens after SST show lower values compared to that before SST, while the corrosion current i_{corr} of the specimens after SST lower. With the processing of SST, the micro cracks and loose corrosion products which can be seen in Fig.2 in the specimen surface lead to the reduction of E_{corr}. According to EDS results, the corrosion products of Cr formed in the corrosion product layer /metal interface could act as a diffusion barrier [3]. This barrier makes the corrosion rate slowdown, which is reflected by the change of $i_{corr.}$ The result is agreed with the EIS results.

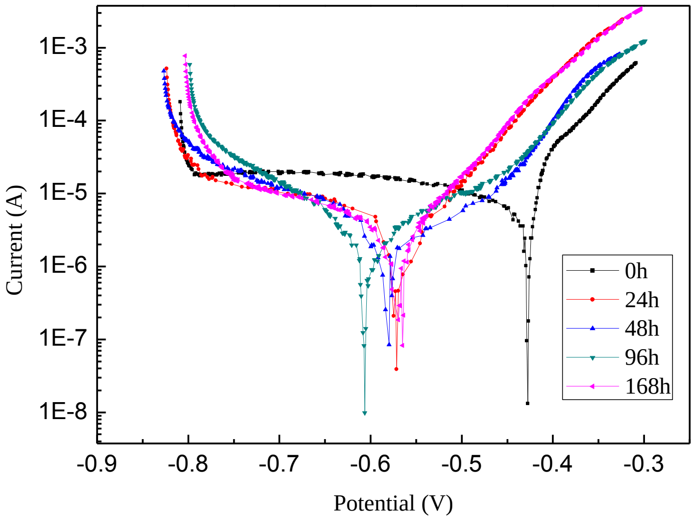

Figure 8. Polarization curves of 23Co14Ni12Cr3Mo after SST for different time

Table 3. Values of parameters calculated from polarization diagrams

Times(h)	Ecorr(V)	Icorr(Acm^{-2})	Ra(Ωcm^2)	Rc(Ωcm^2)
0	-0.428	1.140×10^{-5}	0.0756	-0.516
24	-0.572	5.798×10^{-6}	0.0707	-0.446
48	-0.580	1.644×10^{-6}	0.1660	-0.202
96	-0.606	2.924×10^{-6}	0.1467	-0.135
168	-0.565	3.222×10^{-6}	0.0759	-0.301

3.5 Discussions

From the corrosion products analysis by FT-IR, XRD and XPS, it can be deduced that the corrosion products formed in SST in the initial stage are mainly γ-FeOOH. The reactions [18~20] are shown as Eq(1), Eq(2) and Eq(3).

$$Fe \rightarrow Fe^{2+} + 2e \qquad (1)$$

$$Fe^{2+} + 2H_2O \rightarrow Fe(OH)_2 + 2H^+ \qquad (2)$$

$$4Fe(OH)_2 + O_2 \rightarrow 4\gamma\text{-}FeOOH + 2H_2O \qquad (3)$$

After corrosion for 48h, the oxide of Fe γ-FeOOH transforms to α-FeOOH or Fe_2O_3, which can be formed by Eq(4) or Eq(5). The acicular α-FeOOH can be seen in SEM morphology in Fig.2. And for 96h, the γ-FeOOH are almost transformed to α-FeOOH, which also can be seen in Fig.2 and proved by XRD results.

$$\gamma\text{-}FeOOH \rightarrow \alpha\text{-}FeOOH \qquad (4)$$

$$2\gamma\text{-}FeOOH \rightarrow Fe_2O_3 + H_2O \qquad (5)$$

The XRD and XPS results are shown that the corrosion products of 23Co14Ni12Cr3Mo steel after immersion in SST for 168h are mainly consisted of Fe_3O_4, and Fe_3O_4 can be formed by Eq(6).

$$8\alpha\text{-}FeOOH + Fe^{2+} \rightarrow 3Fe_3O_4 + 4H_2O \qquad (6)$$

From the SEM and EIS results, it can be derived that the pit growth model, which is confirmed by the AFM results. The conformation model of corrosion products of 23Co14Ni12Cr3Mo steel in SST are shown in Fig.9. The surfaces of the same region from the specimen immersed in SST for different time are detected by AFM and the results are shown in Fig.10.

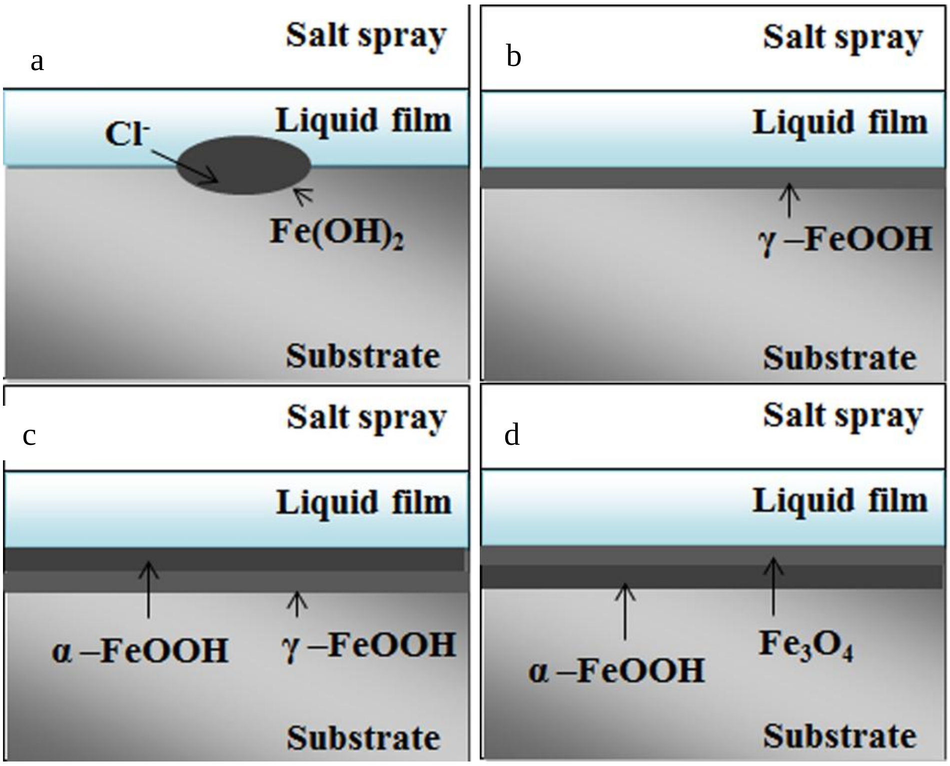

Figure 9. The conformation model of corrosion products of 23Co14Ni12Cr3Mo steel in SST

In initial stage, the chloride ion in the liquid film enters into the substrate, which forms corrosion nucleation. The corrosion source grows up, and forms a bubble which caused by the swell of the corrosion products. It can be found in Fig.2 for 0.15h and 12h, and also in Fig.10 for 0.15h and 12h. The transitionary corrosion products are mainly $Fe(OH)_2$,and the conformation model is shown in Fig.9(a). With the affection of chloride ion, The ion of Fe transforms to $Fe(OH)_2$ quickly, After testing for 24h, the rupture of bubbles leads to undulations in the specimen surface, which can be seen in Fig.10 for 24h. The oxide $Fe(OH)_2$ transforms to γ-FeOOH (Eq(3)). A loose-rugged corrosion product layer is formed, and the conformation model is shown in Fig.9 (b).

As the corrosion goes further, corrosion continuously occurs in the interface of corrosion product and metal, which forms γ-FeOOH, and the outside Oxide γ-FeOOH transforms to acicular α-FeOOH. It appears two layers in the corrosion products, which can be observed in Fig.3 (c).The acicular-rugged morphology is also shown in Fig.10 for 96h, and the conformation model is shown in Fig.9(c).

When the specimen immersed in SST for 168h, the outer layer of α-FeOOH transforms to Fe_3O_4, which seems to be sintered-like (Fig.2 for 168h) and dense (Fig.3(d)), and the inner layer of γ-FeOOH transforms to acicular α-FeOOH, which seems to be looser(Fig.3(d)). The conformation model is shown in Fig.9(d).

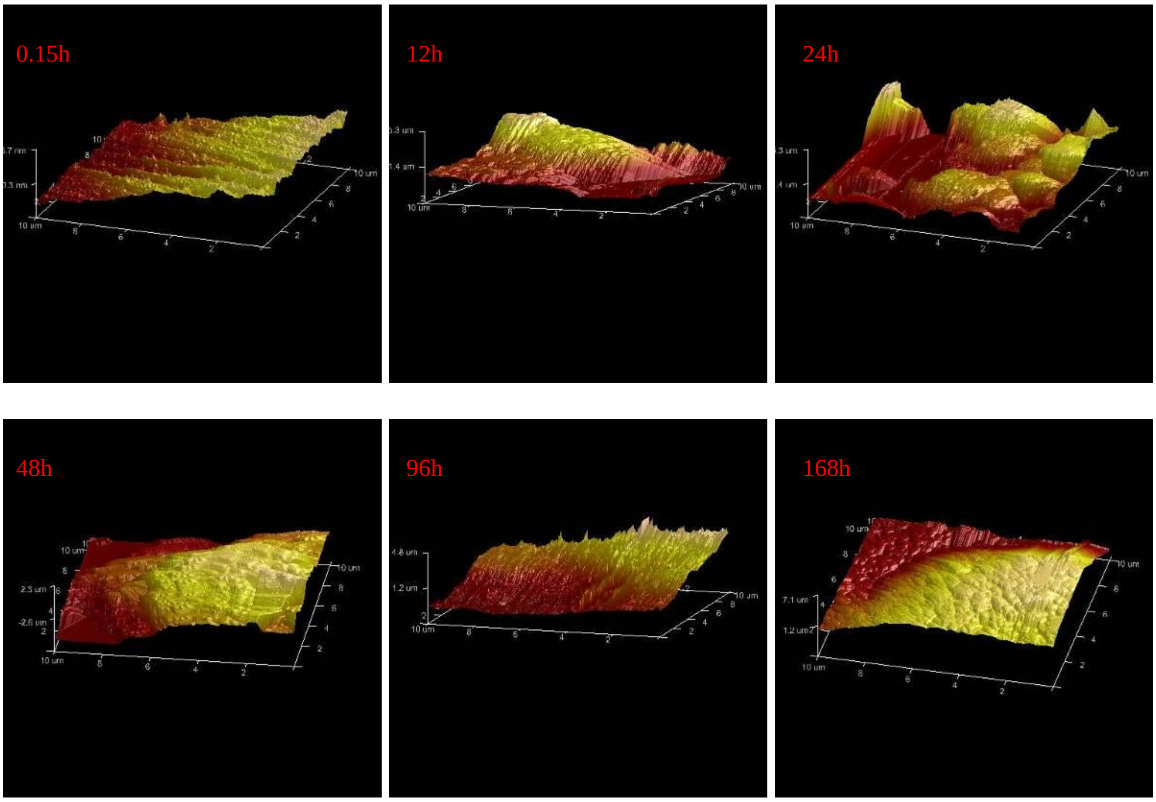

Figure 10. AFM morphologies for different time in SST of 23Co14Ni12Cr3Mo steel

4. CONCLUSIONS

The initial corrosion processes and mechanism of 23Co14Ni12Cr3Mo Ultra-high Strength steel in SST were researched in this work. The conclusions are summarized as follows.

1) The corrosion happens from pits, and forms two layers for inner layer γ-FeOOH and outer layer α-FeOOH for 96h and inner layerα-FeOOH and outer layer Fe_3O_4 for 168h.

2) The corrosion products continuously transform from staked granular to acicular, and finally to sintered. The oxides of Fe are transformed in the form of Fe to γ-FeOOH, to α-FeOOH or Fe_2O_3, and finally to Fe_3O_4.

3) It forms bubbles of $Fe(OH)_2$ for 12h, and the rupture of bubbles forms loose-rugged γ-FeOOH for 24h. The oxide γ-FeOOH transforms to acicular α-FeOOH, while it is also formed in the interface of corrosion product and metal as the corrosion goes further. And for 168h, the inner γ-FeOOH transforms to α-FeOOH and the outer α-FeOOH to Fe_3O_4.

ACKNOWLEDGEMENTS
This work was supported by the National Science Foundation of China (Grant No.51171011).

References

1. D. M. Li, R. P. Gangloff, J. R. Scully, *Metall. Mater. Trans. A*. 35(2004) 849
2. R. L. S. Thomas, J. R. Scully, R. P. Gangloff, *Metall. Mater. Trans. A*. 34(2003) 327
3. Y. B. Hu, C. F. Dong, M Sun, K Xiao, P Zhong, X. G. Li, *Corr. Sci*. 53(2011) 4159
4. Y. W. Lee, R. P. Gangloff, *Metall. Mater. Trans. A*. 38(2007) 2174
5. D. Figueroa, M. J. Robinson, *Corr. Sci*. 52(2010)1593
6. L. F. Wu, S. M. Li, J. H. Liu, M Yu, *J. Cent. South. Univ. T*. 19(2012) 2726
7. A. A. Oehlert, *J. Mater. Sci*. 33(1998) 775
8. M. Sun, K. Xiao, C. F. Dong, X. G. Li, P. Zhong. *J. Mater Eng Perform*. 14(2012)1
9. H. J. Martin, M. F. Horstemeyer, P. T. Wang. *Corros. Sci*. 53(2011)1348
10. W. J. Yang, P. Yang, X. M. Li and W. L. Feng, *Mater Corros*. 63(2012) 401
11. H. C. Liu, H. P. Xu, L. Q. Zhu, J. Z. Liu, X. B. Ye, B.-R. Hu, *Mater Corros*. 62(2011)1
12. Z. C. Ming, S. Patrik, B. Smuel, M. Liu, G. L. Song, A. Atrens, *Corros. Sci*. 51(2009)1277
13. X. L. Hao, J. H. Liu, S. M. Li, M. Yu Mei, *J Aeron. Mater*. 30(2010)67
14. J. H Liu, H. B. Shang, B. W. Tao, S. M. Li, *Mater. Eng*. 8(2004)29
15. M. Yu, Y. Dong, R. Y. Wang, J. Y. Qi, J. H. Liu, S. M. Li, *Mater. Eng*. 1(2012)42
16. A. Nazarov, M. G. Olivier, D. Thierry, *Progr. Org. Coat*. 74(2012)356
17. T. Yamashita, P. Hayes, *Appl. Surf. Sci*. 254(2008)2441
18. Y. Hedberg, M. Norell, P. Linhardt, H. Bergqvist, I. Odnevall Wallinder, Int. *J. Electrochem. Sci.*, 7(2012)11655
19. D. de la Fuente, I. Díaz, J. Simancas, B. Chico, M. Morcillo, *Corros. Sci.*, 53(2011)604
20. L. Hao, S.X. Zhang, J. H. Dong, W. Ke, *Corros. Sci.*, 58(2012)175